Catalysis Today 164 (2011) 209–213

Contents lists available at ScienceDirect

Catalysis Today

journal homepage: www.elsevier.com/locate/cattod

Synthesis of a perovskite $LaNiO_3$ nanocatalyst at a low temperature using single reverse microemulsion

D. Aman [a], T. Zaki [a,*], S. Mikhail [a], S.A. Selim [b]

[a] Catalysis Department, Refining Division, Egyptian Petroleum Research Institute, Nasr city, P.B. 11727, Cairo, Egypt
[b] Chemistry Department, Faculty of Science, Ain Shams University, Cairo, Egypt

ARTICLE INFO

Article history:
Received 28 May 2010
Received in revised form
16 November 2010
Accepted 17 November 2010
Available online 10 December 2010

Keywords:
$LaNiO_3$ perovskite
Reverse microemulsion
Nanocatalyst
Photocatalysis

ABSTRACT

Perovskite $LaNiO_3$ nanoparticles were prepared by a reverse (water/oil) microemulsion method. The microemulsion system consisted of cetyltrimethylammonium bromide, 1-butanol, cyclohexane, and the metal salt solution. The procedure was carried out using aqueous ammonia as the co-precipitating agent. Reverse microemulsions were characterized by measuring the conductivity of the solutions. The dried precipitate was transformed to a perovskite by calcination at 750 °C. Nanosized particles were characterized by thermal analysis, X-ray diffraction, UV-diffuse reflectance spectroscopy, and transmission electron microscopy. The $LaNiO_3$ samples have narrow band gaps and consequently achieved visible-light-induced photocatalytic activity towards the degradation of naphthalene species. The solar photocatalytic activity was found to be influenced by the nanoparticle size.

1. Introduction

Mixed oxides of rare earth elements and *d* transition metals that form perovskite structures (of the form ABO_3) are interesting materials for catalytic applications because of the wide range of elemental compositions that can be prepared as crystalline structures [1], as well as such compounds' characteristically large number of defects, i.e., cationic vacancies [2]. The catalytic activity of such compounds is primarily attributed to the transition metal cation at the B-site, whereas the thermal endurance of the catalyst is largely derived from the rare earth ion at the A-site [3].

$LaNiO_3$ is a cubic or rhombohedrally distorted perovskite-type structure. Rhombohedrally distorted $LaNiO_3$ perovskite is a Pauli paramagnetic [4] compound. As a native p-type semiconductor, $LaNiO_3$ has numerous applications in ferroelectrics, catalytic combustion, conductive thin films, and electrode materials, due to its excellent electric and magnetic properties [5]. $LaNiO_3$ is sensitive to oxygen at elevated temperatures and is unstable in air at temperatures above 860 °C. Specifically, it gradually decomposes to the lower oxide $La_{n+1}Ni_nO_{3n+1}$ above 1200 °C. For these reasons, the synthesis of pure $LaNiO_3$ is restricted to a limited temperature range [6]. $LaNiO_3$ has been shown to be photocatalytically active in the degradation of organic contaminants in water under UV light irradiation and under visible light [5].

It is well known that the properties of materials are related to the preparation method. Single phase $LaNiO_3$ has been synthesized using a number of methods, including conventional ceramic powder technology, sol–gel processing, the Pechini method [3,7], nitrate decomposition, powder co-precipitation [8], powder deposition-aerosol deposition [4], and double-reverse microemulsion [6]. Such techniques generally require high temperatures (in excess of 750 °C), flowing oxygen, and long calcination periods (usually in excess of 16 h) in order to obtain single-phase $LaNiO_3$ [7].

In this study, we have successfully demonstrated the use of the single-reverse microemulsion technique in the preparation of single-phase $LaNiO_3$ nanoparticles that have visible-light-induced photocatalytic activities at a relatively low calcination temperature and short calcination period.

2. Experimental

2.1. Sample preparation

In the single-reverse microemulsion technique, just one reverse microemulsion is used. The reverse microemulsion used for this study consisted of CTAB as surfactant (s), 1-butanol as co-surfactant (cs), and cyclohexane as oil phase (o). In all of the reverse microemulsions, the mass ratio of (cs) to (s) was 1.5. An aqueous solution (w) of $LaCl_3{\cdot}7H_2O$ (0.75 M; Sigma, assay 99.9%) and $Ni(NO_3)_2{\cdot}6H_2O$ (0.75 M; Eastrin Fine Chemicals, Ltd, assay 99%) containing a total metal concentration of 1.5 M was added dropwise

* Corresponding author. Tel.: +202 22736349; fax: +202 22747433.
E-mail address: tamerzakisharara@yahoo.com (T. Zaki).

0920-5861/$ – see front matter © 2010 Elsevier B.V. All rights reserved.
doi:10.1016/j.cattod.2010.11.034

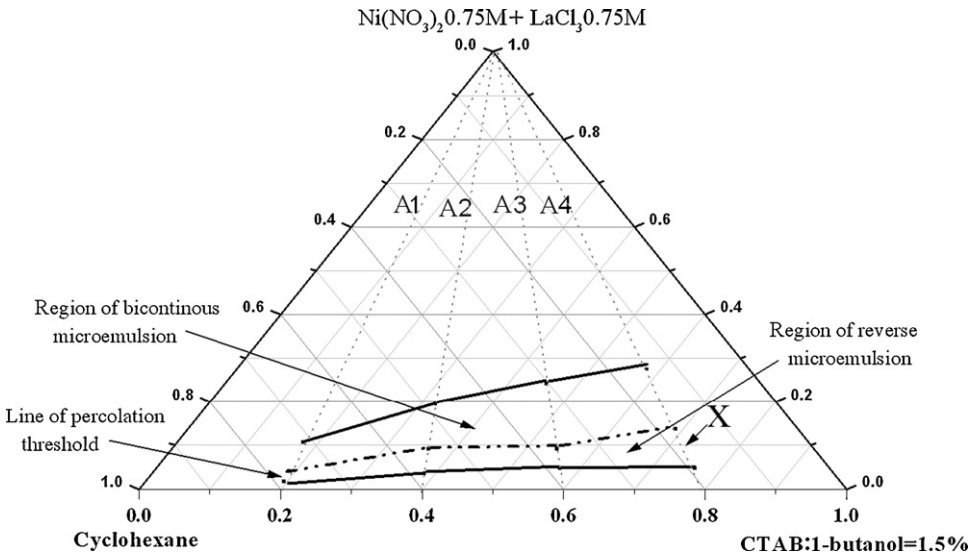

Fig. 1. Phase diagram of the reverse microemulsion system. The conductivity experiments in Fig. 2 were performed along the dotted lines (– – –). The upper bold line (–) corresponds to the upper limits of the experiment. The dashed dotted line (-·-·-·-) corresponds to the maximum of $d\sigma/d\varphi$ curves in Fig. 2 and roughly divides the region of the reverse microemulsion from that of bicontinuous microemulsion. The lower bold line is the approximate limit at the percolation threshold. The point (*X*) corresponds to the composition chosen for the synthesis of perovskite.

to four different ratios of the mixture (s + cs):(o) for mass ratios of 0.2 (A1), 0.4 (A2), 0.6 (A3), and 0.8 (A4).

In Fig. 1, the compositions of the microemulsions used for this study are shown with the aid of a triangle diagram. In this diagram, the initial (s + cs):(o) ratios (0.2, 0.4, 0.6 and 0.8) are shown on the base of the triangle. The addition of $LaCl_3{\cdot}7H_2O$ (0.75 M) + $Ni(NO_3)_2{\cdot}6H_2O$ (0.75 M) took place upwards along the dashed lines A1–A4.

During the addition of the aqueous mixture of salts, $LaCl_3{\cdot}7H_2O + Ni(NO_3)_2{\cdot}6H_2O$, into the (o) + (s) + (cs) mixtures, the conductivity (σ) of the solution was affected. The variation in conductivity was studied using a benchtop Hanna conductivity meter kept at 25 °C with circulating water from a controlled temperature stabilizer. The obtained results are shown in Fig. 2 in the form $\sigma = f(\varphi)$, as well as in the form $d\sigma/d\varphi = f(\varphi)$. The fraction φ is equal to $V_w/(V_w + V_o + V_s + V_{cs})$, where V_w is the volume of aqueous phase, V_o is the volume of oily phase, V_s is the volume of surfactant, and V_{cs} is the volume of co-surfactant. The volume of surfactant (V_s) was not taken into account since the volume of CTAB as a solid was negligibly small.

In the triangular diagram shown in Fig. 1, we have chosen one point (*X*) corresponding to microemulsion A4 for preparing perovskite $LaNiO_3$, designated LNO15. The composition of the chosen point (*X*), as shown in Fig. 1, was (*s*) = 15 g, (*o*) = 31.25 g, (cs) = 7.5 g

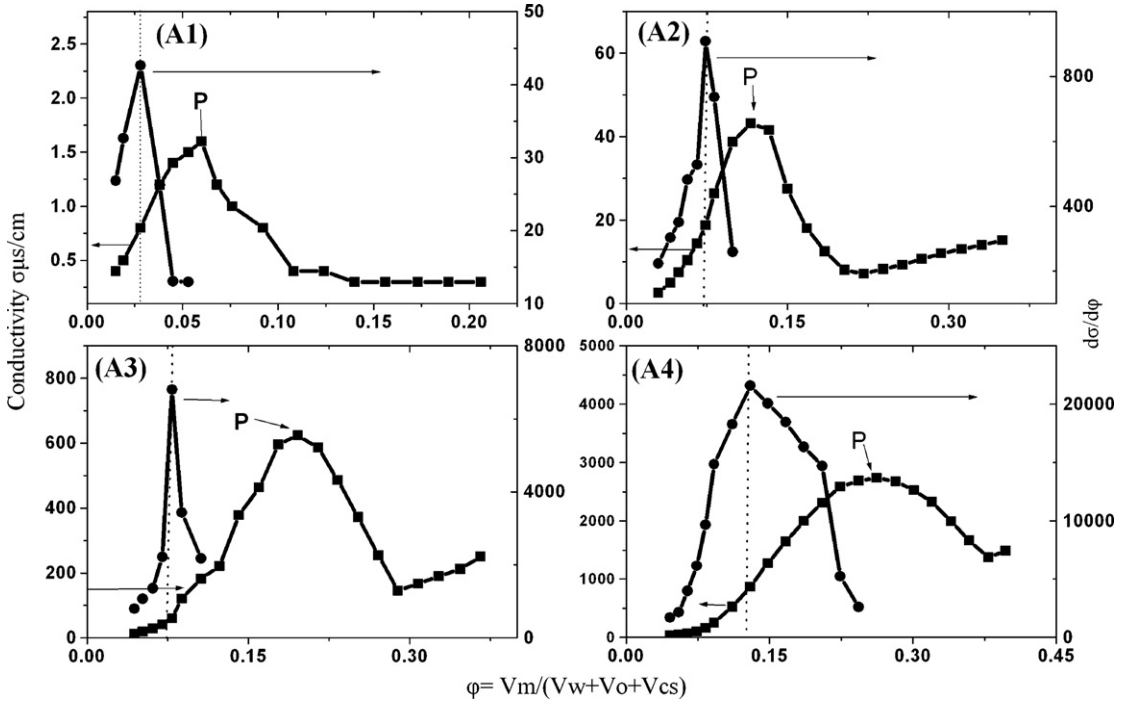

Fig. 2. Variation of the conductivity (σ) of the system by the addition of the aqueous solution (■). The variation of $d\sigma/d\varphi = f(\varphi)$ is also shown. The dashed vertical line separates roughly the reverse region (left) and bicontinuous region (right) of microemulsion (●).

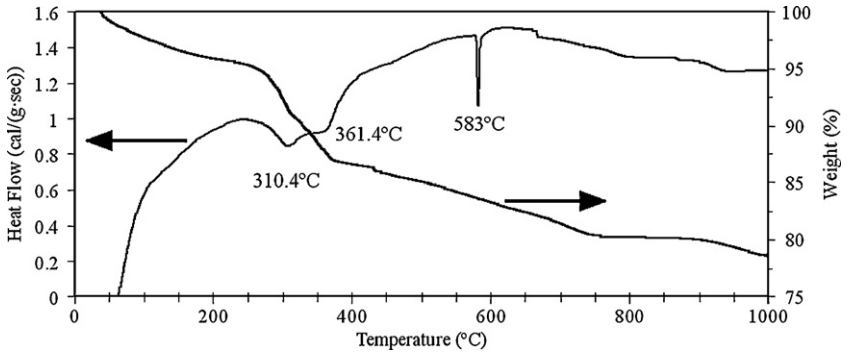

Fig. 3. DTA and TGA curves of a typical LNO15 sample.

and (w) = 13 g. The corresponding perovskite was developed by adding an aqueous NH_4OH solution (4 M) to the vigorously stirred microemulsion A4 as a precipitating agent.

After adding ammonia in excess, a purplish blue precipitate was formed due to the coordination of the nickel species with ammonia. To obtain a good atomic mixing, an excess of deionized water was added to reach a pH value at which the precipitation of mixed solutions might be expected to give a thorough mixture of the hydroxide species. The oxy-hydroxy species of lanthanum is precipitated in the pH range of 8–10 in the presence of ammonium hydroxide as reagent [9]. The precipitation of nickel hydroxide in the presence of an ammonia solution, on the other hand, occurs in stages. The first stage is the precipitation of nickel hydroxide at pH values between 8 and 8.6. The second stage corresponds to the formation of a complex $[Ni(NH_3)_6]^{+2}$ in the pH range of 8.6–10. In the third stage, further precipitation happens above pH 10 [10].

The hydroxide mixture was then filtered, washed alternatively three times with deionized water and an alcohol mixture, and then dried at 100 °C overnight. The dried powder was ground in an agate mortar and calcined at 750 °C for 4 h under atmospheric conditions. The final calcination temperature (750 °C) was selected after thermogravimetric experiment.

Using the above-described experimental conditions, we prepared additional perovskite samples, designated LNO10 and LNO30, using aqueous solutions of $LaCl_3{\cdot}7H_2O$ (0.5 M) + $Ni(NO_3)_2{\cdot}6H_2O$ (0.5 M; total metal concentration = 1.0 M), and $LaCl_3{\cdot}7H_2O$ (1.5 M) + $Ni(NO_3)_2{\cdot}6H_2O$ (1.5 M; total metal concentration = 3.0 M), respectively. The goal of the preparation of these samples was to investigate the influence of total metal precursor concentrations on particle size and optical properties.

2.2. Analytical methods

2.2.1. Thermal analysis (DTA-TGA)

Differential thermal analysis coupled with thermogravimetric analysis of the dried precipitate was recorded simultaneously on an apparatus manufactured by Netsch (Germany). The sample was ground to 20 mesh, and α-alumina was used as a reference inert material. The run was carried out at a heating rate of 10 °C/min.

2.2.2. X-ray diffraction analysis (XRD)

The crystalline structure of the prepared powder was analyzed by X-ray diffractometry (XRD) (X-Pert PRO, PAN analytical, Netherlands) using CuKα radiation in the angular region of $2\theta = 4°–70°$. For phase identification purposes, automatic JCPDS library search and match were used.

2.2.3. Transmission electron microscopy (TEM)

Transmission electron microscopy images were recorded on a JEOL-1400 TEM at 120 kV.

2.2.4. UV-diffuse reflectance spectroscopy (UV-DRS)

Ultraviolet–visible (UV–vis) diffuse reflection spectra of the nanoparticles were recorded using a SHIMADZU, 3101 UV–vis spectrophotometer. The spectra were collected in the 200–800 nm range at room temperature using $BaSO_4$ as a reference.

2.3. Solar photocatalysis

The solar photocatalyzed degradations were carried out from 10.30 am to 12.30 pm during autumn (October–November) under clear sky. The photocatalytic reactions were made in Pyrex glass tubes (covered by transparent thin film) filled with a mixture of 10 mL fresh solutions of naphthalene of desired concentrations (40–10,000 ppm) and catalyst powder (0.1 g). During the reaction, the solution was magnetically stirred. The solution was analyzed with high-performance liquid chromatograph (HPLC, Waters apparatus 600E), which was equipped with a supelcosil LC-PAH column, and had been using a mixture of water and acetonitrile (2:3) as the eluent. The naphthalene absorption was monitored using dual UV absorbance detector Waters 2487 adjusted at 254 nm.

3. Results and discussion

Fig. 2 shows that a gradual increase in φ (aqueous ratio) results in an increase in conductivity (σ), because both the number and the size of the micelles increase. The variation of $d\sigma/d\varphi = f(\varphi)$ is also shown in Fig. 2. The conductivity maximum can be attributed to the saturation of the micelles and the percolation phenomenon [11]. When more water was added to the system, it led to a phase separation, and conductivity was lowered. The point (P) in Fig. 2 is the saturation point. The larger the region between the initial and maximum conductivity, the greater the W/O micelle region, and the better the system is for producing a microemulsion [12].

The reaction process during the steps of co-precipitation and the thermal treatment can be described with the following equations:

$$LaCl_3 + Ni(NO_3)_2 + 5NH_4OH \rightarrow La(OH)_3 + Ni(OH)_2 + 2NH_4NO_3 + 3NH_4Cl \quad (1)$$

$$2La(OH)_3 + Ni(OH)_2 \rightarrow La_2O_3 + NiO + 4H_2O \quad (2)$$

$$La_2O_3 + 2NiO + \frac{1}{2}O_2 \rightarrow LaNiO_3 \quad (3)$$

Typical thermogravimetric analysis (TGA) and differential thermal analysis (DTA) curves of LNO15 (Fig. 3) are in agreement with the combined thermal behaviors of lanthanum hydroxide and nickel hydroxide. The thermal profile shows a small loss in weight (~5%) due to elimination of residual water and surfactant in the range 55–230 °C. The TG curve also shows that decomposition of $Ni(OH)_2$ and $La(OH)_3$ occurred between 231 °C and 745 °C. The

weight loss was about 15.13 wt%, which is in agreement with the theoretical value of 15.24 wt% caused by the loss of four molecules of water (Eq. (2)). The TG curve showed an abrupt weight loss at around 310 °C, accompanied by two endothermic effects at 310 °C and 361 °C for $Ni(OH)_2$ and $La(OH)_3$, respectively, as shown on the DTA curve. The endothermic effect at 310 °C can be attributed to the decomposition of the nickel hydroxide into its oxide [13,14]. The second endothermic effect at 361 °C may be due to the decomposition of the lanthanum hydroxide into lanthanum hydroxide oxide (LaOOH) [15,16]. The abrupt weight loss followed by a slower loss that ended at about 750 °C, accompanied by sharp endothermic effects at 580 °C on the DTA curve, may be due to the formation of lanthanum oxide [15,16].

Fig. 4 represents the evolution of the peaks in the XRD pattern for LNO10 powders calcined at various temperatures, LNO15 and LNO30 powders calcined at 750 °C. LaNiO2.7 and LaNiO2.5 are appeared for calcined LNO10 at 400 and 600 °C. These oxygen deficient phases are detected according to JCPDS files Nos. 37-0928 and 82-0556. Also, the presence of free nickel oxide and lanthanum oxide are observed at these temperatures. At temperature 750 °C, strong peaks characteristic of a rhombohedral $LaNiO_3$ phase were observed at d-spaces 2.735 Å, 2.701 Å, and 1.926 Å, without any trace of an impurity phase. This phase was identified according to JCPDS file No. 33-0711. Fig. 4 shows that the crystallinity increase in the sequence: LNO10 > LNO15 > LNO30. Also, traces of free nickel oxide and lanthanum oxide are observed in LNO30 powder.

The use of the reverse microemulsion technique may allow for the preparation of single-phase rhombohedral $LaNiO_3$ at a low calcination temperature. In this technique, the surfactant molecules aggregate spontaneously, with water located in the core of the aggregates forming nanometer-sized water droplets that act as reactors for the formation of perovskite particles. Due to the dynamics of the system, the water-in-oil droplets are very rapidly mixed, leading to the formation of the perovskite particles by precipitation inside the microemulsion droplets. Accordingly, the reaction kinetics are controlled by the diffusion and collisions between the metal and hydroxide ions in the microemulsions [6]. As soon as the metal hydroxide particles are formed, the surfactant molecules prevent them from coalescing, and hence the precipitation process is slow, extending over a period of several hours. The perovskite can then be formed at a low calcination temperature, due to the homogeneous mixing of the metals and to the very small size of the primary particles [17].

It is obvious from the TEM analysis in Fig. 5 that the shape of the particles is mostly square, and their particle size distribution is also uniform. In general, the perovskite $LaNiO_3$ particles are crystalline, and the particle sizes increased as the total concentration of metal precursors increased. Fig. 5 shows that the grain sizes of the LNO10 sample are 11–21 nm, whereas the grain sizes of the LNO30 sample are 30–100 nm.

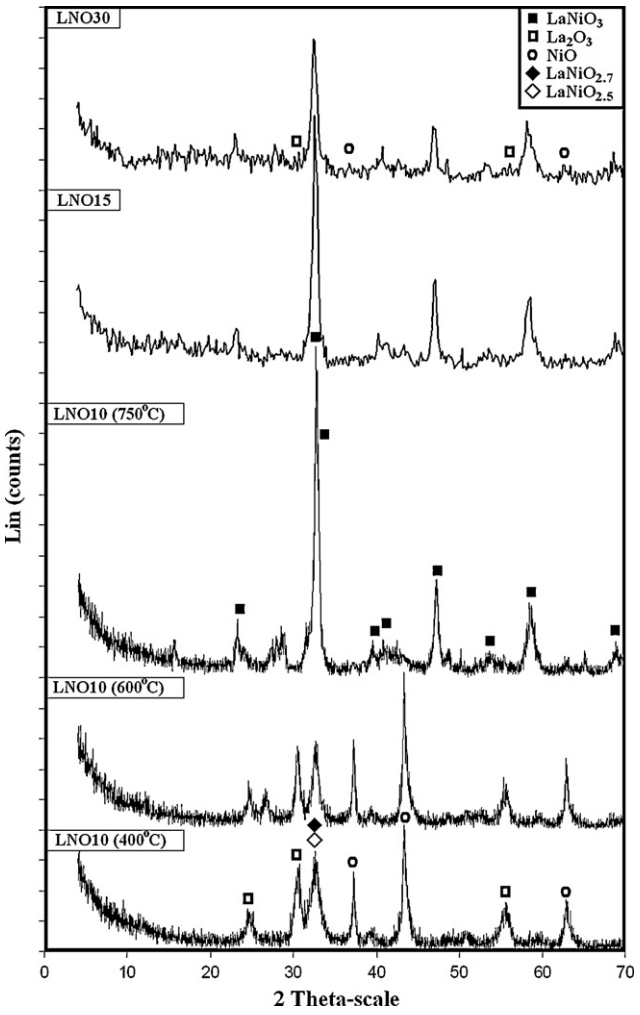

Fig. 4. X-ray diffraction patterns of LNO10 sample calcined at different temperatures, LNO15 and LNO30 samples calcined at 750 °C.

Fig. 6 shows diffuse reflectance spectra of $LaNiO_3$ nanoparticles. The absorbance increases as grain size of the perovskite nanoparticles decreases, with LNO10 (11–21 nm) showing the highest absorbance. The optical band-gap energy (E_g) for the $LaNiO_3$ nanoparticles was evaluated by the extrapolation method (inset of Fig. 6) [18,19]. The absorption edges of the $LaNiO_3$ samples extend to the visible light region. The LNO30 sample shows band gap energy narrowing to about 2.51 eV, which can effectively absorb visible light. The calculated value of the band gap agrees well with the literature value (2.26 eV) [5].

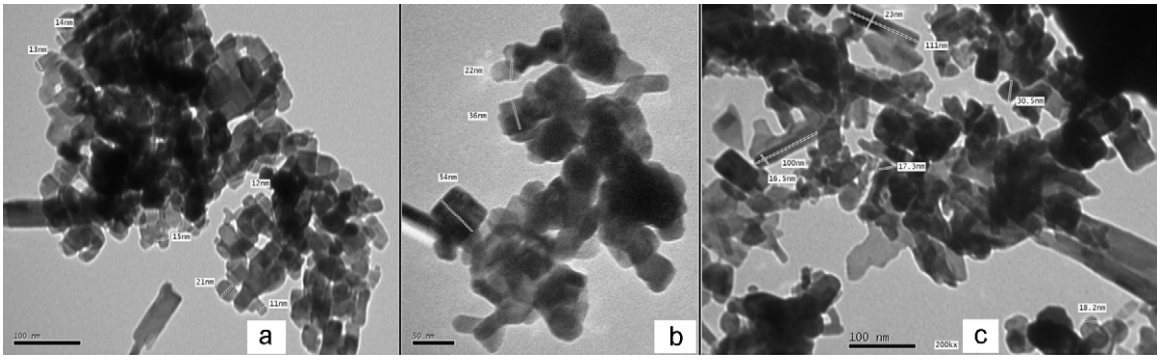

Fig. 5. TEM image of (a) LNO10, (b) LNO15 and (c) LNO30 samples.

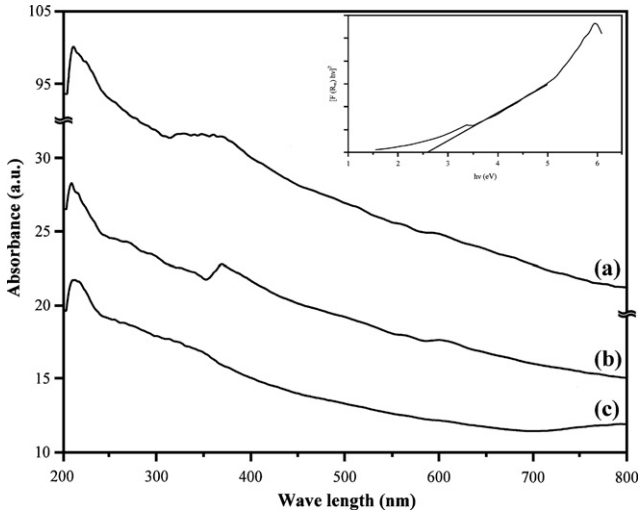

Fig. 6. Kubelka-Munk conversion spectra of (a) LNO10, (b) LNO15 and (c) LNO30 samples. Inset: band-gap energy of LNO15 sample.

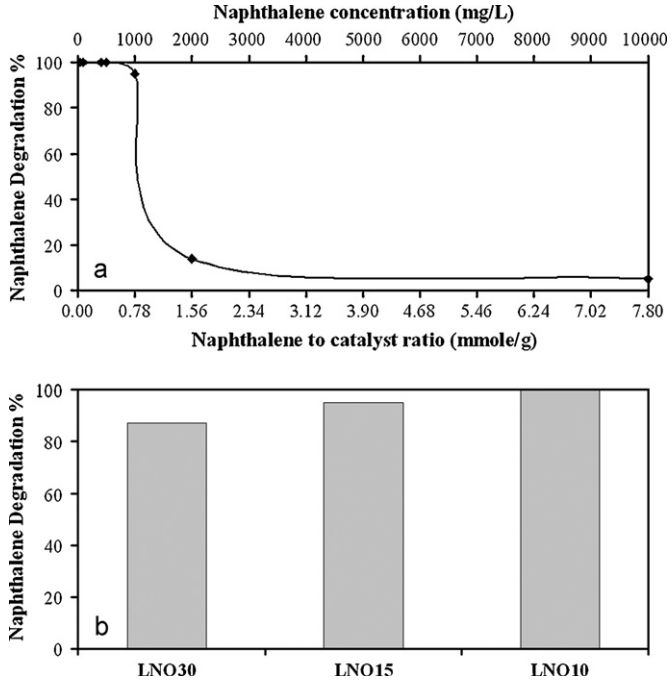

Fig. 7. Solar photocatalytic degradation of naphthalene species using (a) LNO15 catalyst with different naphthalene concentrations and (b) different $LaNiO_3$ catalysts with 1000 ppm naphthalene solution.

The visible-light-induced photocatalytic activity of $LaNiO_3$ powders were investigated based on the photodegradation of naphthalene. Upon irradiating the naphthalene solution without the catalyst, partial conversion was observed. The degradation percentage was calculated according to the final concentrations of naphthalene species in the presence and absence of the catalyst. Fig. 7a shows the evolution the influence of the concentration of naphthalene solution of the catalytic activity of LNO15. As it can be seen, the solar photocatalytic activity of LNO15 sample increased sharply as the naphthalene concentration decreased from 2000 to 1000 ppm. LNO15 achieved complete photodegradation for the naphthalene species at concentration 500 ppm within 120 min (10.30 am to 12.30 pm). Fig. 7b shows the solar photocatalytic degradation of naphthalene species (1000 ppm) using different $LaNiO_3$ catalysts. LNO10 performed the highest activity (100%) while LNO30 achieved about 87% degradation. As the photocatalytic activities of the catalysts are highly corresponding to the surface structure and crystallinity [20], the previous mentioned results can be attributed to the high crystallinity of LNO10 sample (Fig. 4) and its high optical absorbance capacity (Fig. 6) which accompanied the decrease in average grain size of $LaNiO_3$ nanoparticles (Fig. 5).

4. Conclusion

$LaNiO_3$ perovskite has been synthesized by a single-reverse microemulsion process. A pure rhombohedral $LaNiO_3$ was readily formed at a low calcination temperature (750 °C) and short calcination period (4 h). The single-reverse microemulsion process results in a lower $LaNiO_3$ crystallization temperature than other precipitation methods. The synthesized cubic nanoparticles have a narrow band gap. This property allows $LaNiO_3$ perovskite to absorb visible light, thus generating charge carriers and leading to solar photocatalytic activity. LNO10 catalyst showed the highest activity towards the photodegradation of naphthalene due to its high crystallinity and high optical absorbance capacity.

References

[1] M. Wallin, N. Cruise, U. Klement, A. Palmqvist, M. Skoglundh, Colloids Surf. A. 238 (2004) 27–35.
[2] I.V. Krylova, Russ. Chem. Bull. Int. Ed. 51 (2002) 46–53.
[3] J.D.G. Fernandes, D.M.A. Melo, A.M.G. Pedrosa, M.J.B. Souza, D.K.S. Gomes, A.S. Araujo, React. Kinet. Catal. Lett. 84 (2005) 3–9.
[4] J.-J. Choi, J. Ryu, B.-D. Hahn, W.-H. Yoon, D.-S. Park, J. Am. Ceram. Soc. 91 (2008) 2756–2758.
[5] Y. Li, S. Yao, W. Wen, L. Xue, Y. Yan, J. Alloys Compd. 491 (2010) 560–564.
[6] L.M. Gan, L.H. Zhang, H.S.O. Chan, C.H. Chew, B.H. Loo, J. Mater. Sci. 31 (1996) 1071–1079.
[7] J.D.G. Fernandes, D.M.A. Melo, L.B. Zinner, C.M. Salustiano, Z.R. Silva, A.E. Martinelli, M. Cerqueira, C.A. Júnior, E. Longo, M.I.B. Bernardi, Mater. Lett. 53 (2002) 122–125.
[8] S. Sugunan, V. Meera, React. Kinet. Catal. Lett. 62 (1997) 327–332.
[9] K. Normana, M.A. Morris, J. Mater. Process. Technol. 92/93 (1999) 91–96.
[10] M.B.J.G. Freitas, R.K. Silva e Silva, D.M. Anjos, A. Rozário, P.G. Manoel, J. Power Sources 165 (2007) 916–921.
[11] A. Košak, D. Makovec, M. Drofenik, Phys. State Solid C. 1 (2004) 3521–3524.
[12] F. Li, C. Vipulanandan, K.K. Mohanty, Colloids Surf. A. 223 (2003) 103–112.
[13] C-F. Kao, C.-L. Jeng, Ceram. Int. 25 (1999) 375–382.
[14] C-F. Kao, C-L. Jeng, Ceram. Int. 26 (2000) 237–243.
[15] A. Neumann, D. Walter, Thermochim. Acta 445 (2006) 200–204.
[16] M. Mazloumia, N. Shahcheraghia, A. Kajbafvala, S. Zanganeha, A. Laka, M.S. Mohajerania, S.K. Sadrnezhaad, J. Alloys Compd. 473 (2009) 283–287.
[17] A. Giannakas, A. Leontiou, A. Ladavos, P. Pomonis, Appl. Catal. A 309 (2006) 254–262.
[18] R.S.G. Ferreira, P.G.P. de Oliveira, F.B. Noronha, Appl. Catal. B. 29 (2001) 275–283.
[19] L. Jia, J. Li, W. Fang, J. Alloys Compd. 489 (2010) L13–L16.
[20] Y. Zhang, G. Li, Y. Wu, Y. Luo, L. Zhang, J. Phys. Chem. B. 109 (2005) 5478–5481.